



Bidirectional reflectance capabilities of the NIST Robotic Optical Scattering Instrument

HEATHER J. PATRICK,*  CATHERINE C. COOKSEY,  THOMAS A. GERMER, MARIA E. NADAL, AND CLARENCE J. ZAROBILA

Sensor Science Division, National Institute of Standards and Technology, 100 Bureau Dr., Gaithersburg, Maryland 20899, USA

*Corresponding author: heather.patrick@nist.gov

Received 24 June 2021; revised 25 August 2021; accepted 30 August 2021; posted 9 September 2021 (Doc. ID 435117); published 27 September 2021

The National Institute of Standards and Technology (NIST) Robotic Optical Scattering Instrument (ROSI) serves as the national reference instrument for specular and diffuse bidirectional reflectance measurements in the ultraviolet to short-wave infrared wavelength regions. This paper gives a comprehensive overview of the design, operation, and capabilities of ROSI. We describe measurement methods for diffuse and specular reflectance, identify and quantify the elements of the uncertainty budget, and validate the reflectance scale through comparison with NIST's previous reference instrument, the Spectral Tri-function Automated Reference Reflectometer. Examples of the range of ROSI's capabilities, including the limits for low-reflectance measurements and a research application using out-of-plane measurements of bidirectional reflectance for remote sensing reference reflectors, are also covered.

<https://doi.org/10.1364/AO.435117>

1. INTRODUCTION

Since the early 1990s, the National Institute of Standards and Technology (NIST) has provided SI-traceable measurements of bidirectional reflectance, that is, reflectance at a specific illumination direction and into a specific viewing direction, for both specular and diffuse materials. These measurements were historically provided by the Spectral Tri-function Automated Reference Reflectometer (STARR) [1]. On STARR, while specular measurements were always provided over the ultraviolet to shortwave infrared (UV-SWIR) from 250 to 2500 nm, the instrument's capabilities for diffuse reflectance, described by the bidirectional reflectance distribution function (BRDF, f_r) or reflectance factor (RF, R) [2], were initially limited to the 250 to 1100 nm spectral range of the silicon photodiode. STARR's measurements have also been limited to in-plane geometries, where the viewing angle is constrained to lie within the plane formed by the incident angle and the sample normal. Over time, to address the needs of the remote sensing community and other stakeholders, STARR's capabilities for $0/45^\circ$ reflectance factor (incident angle θ_i of 0° and viewing angle θ_v of 45°) were expanded into the SWIR [3], and NIST's scale for bidirectional diffuse measurements was validated through a bilateral comparison [4]. Additionally, NIST and other national metrology institutes recognized the growing need for out-of-plane spectral BRDF measurements. Goniometric instruments (sometimes referred to as goniospectrophotometers) were developed based on nested, orthogonally mounted rotation stages [5] and robotic arms [6,7]. To continue to meet the needs

of its stakeholders, NIST began developing the next-generation reference instrument for specular and bidirectional reflectance, the Robotic Optical Scattering Instrument (ROSI) [8]. ROSI's robotic goniometer expands upon the previous goniometer's capabilities by enabling out-of-plane measurements, with the combination of robotic arm sample holder and the rotation of the receiver arm allowing reflectance measurements at nearly any combination of incident and viewing angles. This is particularly important, for example, in applications such as remote sensing, where a diffuse reflector may be used as a reflectance standard with the viewing angle rotated azimuthally out of the plane formed by the incident angle and sample normal [9].

The initial ROSI system was introduced in 2013 with the robot-based goniometer, a supercontinuum-fiber-laser-based tunable light source operating from 450 to 2450 nm, and a preliminary uncertainty budget [8]. In the past several years we have made key refinements that have enabled the transfer of all bidirectional reflectance calibrations from STARR to ROSI. To extend the UV operation of ROSI into the 250–450 nm range, we added a high-brightness xenon-laser-driven light source that can be coupled into the monochromator to cover wavelengths that are not supplied by the supercontinuum source. We have thoroughly characterized the uncertainty budget, refining the estimate of solid angle uncertainty, which is one of the largest contributors to uncertainty in diffuse bidirectional measurements. Finally, we have validated reflectance measurements on ROSI through comparisons with STARR for specular and

diffuse calibrations. The advances in ROSI have enabled diffuse bidirectional calibrations in the SWIR to be offered at the same geometries as those in the UV-NIR, have increased the light source flux to reduce signal noise and enable measurements of lower reflectance samples, and have allowed measurements to be extended to out-of-plane geometries.

2. MEASUREMENT METHOD

ROSI makes absolute measurements of bidirectional specular and diffuse reflectance; that is, the reflectance is determined relative to the flux in the incident beam, without need for a reference sample. ROSI employs a narrowband, tunable light source and broadband detectors. For any measurement, there are two positions for the detector: incident and sample. In the incident position, the sample is translated out of the beam, and the detector is rotated to collect the entire radiant flux of the illumination beam. In the sample position, the sample is translated into the beam and rotated to the designated illumination angle, and the detector is rotated to collect the reflected radiant flux at the designated viewing angle. Signals from the incident and sample positions, S_i and S_r , are proportional to the incident and reflected radiant fluxes, respectively. For specular measurements, the sample reflectance is simply the ratio of S_r to S_i , and in-plane coordinates describe the measurement geometry sufficiently. For diffuse reflectance, coordinates including the polar and azimuthal angles of illumination and viewing relative to the sample normal are needed, and the solid angle over which the reflected light is collected must be accounted for. Sections 2.A and 2.B describe the geometries and methods used in specular and diffuse reflectance measurements. Details of the system components, including the tunable light source, robot goniometer, and receiver with broadband detectors, are given in Section 3.

A. Specular Reflectance

For specular reflectance, measurements are described by the in-plane geometry shown in Fig. 1. Measurements are designated as θ_i/θ_r , where θ_i is the illumination angle and θ_r is the viewing angle and where both are expressed in degrees.

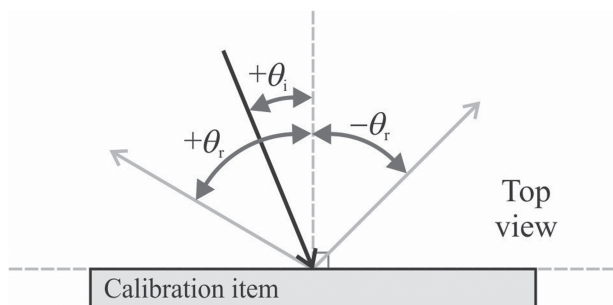


Fig. 1. Top view of illumination and viewing angles θ_i and θ_r , respectively, for an in-plane geometry reflectance measurement. The “+” and “-” signs in the figure indicate where θ takes on positive or negative values with respect to the top and normal of the calibration item. The top of the calibration item is specified by a fiducial or by other means to fully specify the measurement geometry.

While Fig. 1 shows the general geometry for in-plane measurements, specular measurements are further restricted to the case where θ_i and θ_r are equal in magnitude and are on opposite sides of the sample normal, for example, $6/ -6$. The sample specular reflectance ρ is calculated using Eq. (1):

$$\rho = \frac{S_r}{S_i}. \tag{1}$$

B. BRDF and Reflectance Factor

Two principal measurement methods exist for BRDF: the over-illumination method, in which the whole sample is illuminated with uniform irradiance and the scattered radiance is measured, and the under-illumination method, in which a relatively small spot on the sample is illuminated and a receiver collects all the light scattered into a known solid angle [10]. While there are advantages to both methods, ROSI employs the under-illumination method because it enables the instrument to be used for both specular and diffuse measurements and because it is relatively efficient in its use of light. Figure 2 shows the coordinate system for BRDF measurements, with the conventions for θ_i , ϕ_i , θ_r , and ϕ_r . In ROSI, the incident beam illuminates a small spot on the sample at a selectable polar angle of incidence θ_i and azimuthal angle ϕ_i , and a receiver collects the reflected flux within a solid angle Ω at polar and azimuthal scattering angles θ_r and ϕ_r . When both ϕ_i and ϕ_r are 0° or 180° , the geometry of Fig. 2 reduces to the in-plane case shown in Fig. 1, taking the convention that θ is positive (negative) when ϕ is 0° (180°).

The diffuse reflectance is described by the BRDF f_r . The formal definition of the BRDF is the reflected radiance normalized by the incident irradiance for a uniform sample, uniformly illuminated [2]. In the under-illumination method, this has been shown to be equivalent to [11]

$$f_r = \frac{S_r}{S_i \cdot \Omega'}, \tag{2}$$

where Ω' is the effective projected solid angle and is given by the solid angle Ω subtended by the detector aperture, multiplied by the surface projection $\cos \theta_r$, and correction factors that are discussed in Section 4.B. It should be understood that while not explicitly called out in Eq. (2), the BRDF of all materials varies

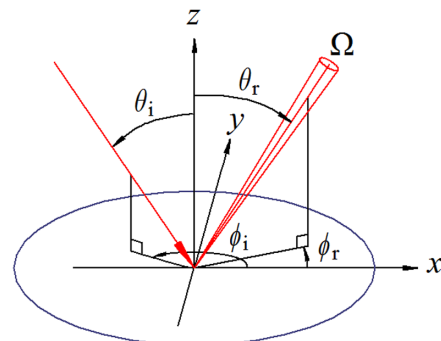


Fig. 2. Illustration of the angles used to describe generalized out-of-plane measurement geometries, where the directions of illumination and viewing are specified with azimuthal and polar angles relative to the sample surface normal.

with θ_i , ϕ_i , θ_r , and ϕ_r , as well as polarization and wavelength of the incident light. For a nonuniform sample, it will also vary with illuminated position, but we are generally concerned with samples that are uniform over the illuminated area.

The BRDF f_r in Eq. (2) has units of inverse steradians (sr^{-1}). A second quantity often used to describe diffuse reflectance is the directional-directional reflectance factor R , which is the unitless ratio of the BRDF at a given incident and viewing geometry relative to the BRDF of a perfectly reflecting diffuser (PRD) and is given by

$$R = \pi f_r. \quad (3)$$

The PRD is a theoretical ideal diffuse surface that reflects incident radiation without losses, completely diffusely, and with a Lambertian directional distribution. The BRDF of a PRD is a constant equal to $1/\pi$, independent of angles, wavelength, and polarization. Hence the reflectance factor shown in Eq. (3) will have values near unity for nearly Lambertian highly reflecting samples.

3. SYSTEM DESCRIPTION

Figure 3 shows a schematic of ROSI. The system can be functionally divided into three parts: the light source, the goniometer, and the receiver. In the following subsections, we will describe each of these parts.

A. Tunable Light Source

The ROSI light source is designed to provide tunable, quasi-monochromatic illumination to the sample with well-defined

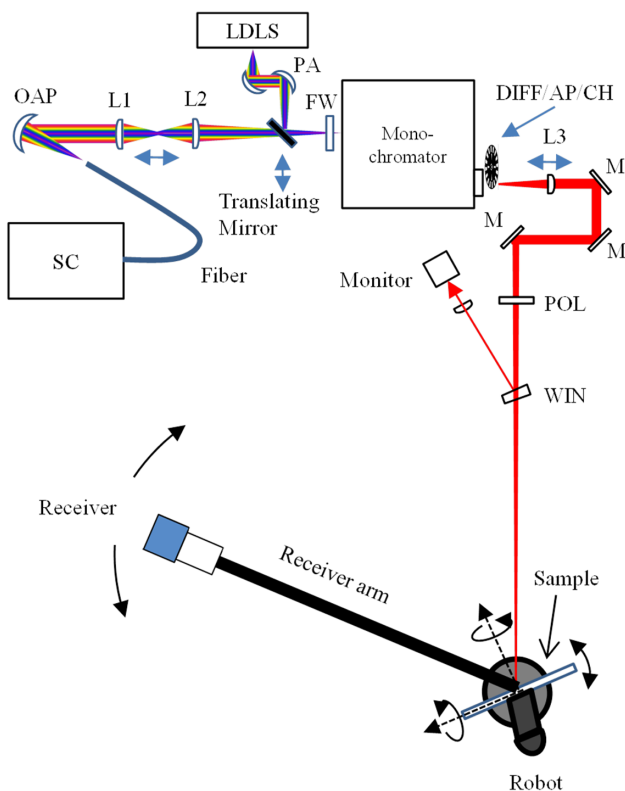


Fig. 3. Schematic of the ROSI instrument. Acronyms are defined in the text.

collimation. The source is based upon two broadband light sources: a supercontinuum fiber laser source, Fianium Model SC450-6-LW, with broadband output from 450 to 2400 nm and labeled SC in the figure, and a high-brightness laser-driven light source, Energetiq Model EQ-99-PLUS-NA, with output from roughly 220 nm into the short-wave infrared and labeled LDLS in the figure. (Certain commercial equipment, instruments, or materials are identified in this paper in order to specify the experimental procedure adequately. Such identification is not intended to imply recommendation or endorsement by the National Institute of Standards and Technology, nor is it intended to imply that the materials or equipment identified are necessarily the best available for the purpose.) The source is selected via a translating mirror. For the SC, an off-axis parabola (OAP) collimates the fiber output and is followed by two translatable lenses L1 and L2. These two lenses move according to the selected wavelength to account for chromatic dispersion in the optics and the fiber to ensure high-throughput coupling into the monochromator [12]. For the LDLS, a periscope assembly (PA) consisting of a pair of reflective off-axis parabolas are used to match the source to the monochromator. The single-grating monochromator (Newport Model MS257) includes an order-sorting filter wheel (FW), toroidal optics, and a four-grating turret with different gratings optimized for different parts of the wavelength range. At the monochromator output, a fused-silica diffuser (DIFF) precedes a 500 μm diameter round aperture (AP). The diffuser helps to expand the focused spot to fill the aperture. The output from the aperture is quasi-monochromatic light with fixed full width at half-maximum bandwidth of about 14 nm, tunable from 250 to 2400 nm. Typically, the LDLS is used for wavelengths from 250 to 500 nm, and the SC is used above 500 nm up to 2400 nm. The optical power reaching the sample is typically tens of microwatts when using the LDLS and hundreds of microwatts with the SC source.

After the monochromator, a lens (L3) images the aperture (AP) to the center of the goniometer, resulting in an incident beam with a 10 mm circular cross section at the sample position. The incident beam is quasi-collimated, with a half-angle from the edge of the exit pupil of L3 to the goniometer center of 0.37° . Mirrors (M) enable alignment of the source to the goniometer, and automated translation of L3 ensures that the focus remains at the center of the goniometer over the broad wavelength range of the source. A chopper (CH) operating at 75 Hz allows lock-in detection of received light during measurements. We control the polarization of the light delivered to the goniometer using a Moxtek ultra-wideband wire-grid linear polarizer (POL) such that linearly polarized light with a selectable rotation angle is delivered to the sample. Finally, a pick-off window (WIN) reflects a small portion of the source output (8% nominal) and directs it to a power monitor that consists of a lens, integrating sphere, and silicon and extended-range indium gallium arsenide (EIGA) detectors attached to the sphere. Use of the monitor allows us to compensate for any fluctuations in the source power during measurements.

B. Robotic Goniometer and Receiver

Figure 4 shows a photo of the robot and receiver arm that are represented schematically in Fig. 3. An industrial six-axis robotic

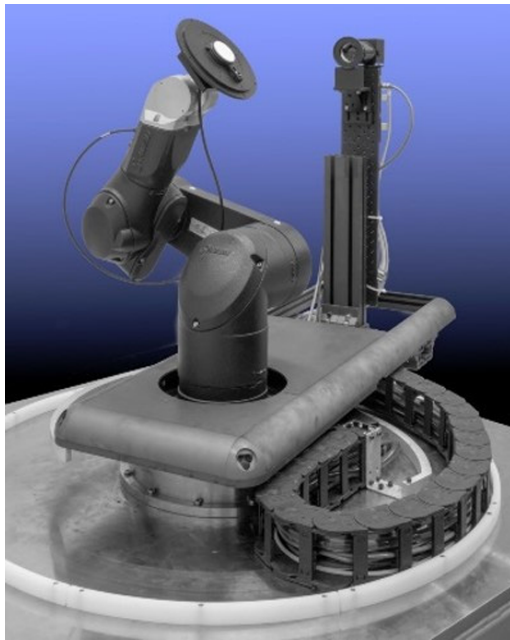


Fig. 4. Robot and receiver arm, shown positioned for an out-of-plane scattering measurement of a white diffuse sample.

arm (Staubli TX60) holds the sample and provides rotation and translation of the sample. The receiver is mounted on an arm connected to a rotation stage that moves the receiver about a vertical axis around the central sample position. The robot is programmed such that the area of interest on the sample face is held at the goniometer center, which is defined by the intersection of the incident light beam and the robot waist rotation axis. The robot and detector arm rotation stage are aligned such that the axis of rotation of the receiver arm is aligned with the robot waist axis. In this way, a constant distance is maintained between the center of the illuminated area of the sample and the center of the precision aperture of the receiver.

Samples are held using an integrated vacuum chuck or mechanically attached to the sample holder. This allows most samples to be held by the back face, so that the receiver view of the front of the sample is unobstructed and the sample face does not need to be touched. The thickness of the sample is input to the robot software to bring the sample face to the goniometer center. Wedged samples can also be accommodated in software, provided the direction of the wedge is known. Alternatively, samples that cannot be mounted by the back face can be provided with an adapter that then mounts to the sample holder.

The receiver consists of a precision aperture followed by a CaF_2 lens with appropriate focal length to image a 60 mm diameter field of view at the sample onto a 10 mm image at the detector plane. The 60 mm field of view enables the entire illuminated area on the sample, which spreads to an ellipse for nonzero θ_i , to under-fill the receiver field stop for θ_i up to 80° . The focus quality of the image varies with wavelength due to chromatic dispersion but has been determined through optical modeling to be sufficient for the measurements. Two different detectors are used: an ultraviolet-enhanced silicon photodiode and an EIGA photodiode mounted on a small integrating sphere. A translator allows either detector to be positioned

Table 1. Typical Source and Detector Combinations for Measurements

Wavelength Range	Source	Detector
250 to 500 nm	LDLS	Silicon photodiode
>500 to 1050 nm	SC	Silicon photodiode
>1050 to 2400 nm	SC	EIGA photodiode on integrating sphere

behind the precision aperture and lens assembly at the detector plane, with either the 10 mm diameter of the silicon photodiode, or the 10 mm diameter entrance port of the integrating sphere serving as the image field stop. In the original receiver design [8], both photodiodes were mounted on the integrating sphere, but after expanding the system to UV wavelengths using the LDLS, the combination of lower spectral power density from the LDLS compared to the SC source and lower sphere throughput at UV wavelengths necessitated a switch to direct illumination for the silicon photodiode.

ROSI performs absolute measurements of BRDF and reflectance, meaning that the receiver must be able to measure both the incident power and the scattered power. During the incident power measurement, the robot moves the sample clear of the incident beam, the receiver faces the incident beam, and the spot size of the incident beam under-fills the precision aperture. In this case, the lens focuses the incident beam to the detector. Typically, the silicon photodiode is used for measurements between 250 to 1050 nm, while the EIGA detector is used from 1050 to 2400 nm. Table 1 shows the typical combinations of light source and detector used as a function of operating wavelength. Note that each source and detector combination can be operated over some range outside of the nominal wavelengths given in the table. This allows operating wavelengths to be adjusted for convenience and to check consistency between measurements with different source and detector combinations.

Both the silicon and EIGA photodiodes are amplified using current-to-voltage amplifiers with multiple, adjustable gain settings. The 75 Hz AC-modulated signals are collected using lock-in amplifiers. The lock-in measures only signals in a narrow band around the chopping frequency and at the correct phase relative to the chopper. The use of lock-in detection minimizes the sensitivity to background light in the room and vastly improves the signal-to-noise ratio compared to unmodulated detection methods [13]. The light source, robotic goniometer, and signal collection are fully automated using a LabView program. Table 2 summarizes the features and capabilities of the system.

A few notes are in order regarding the intended sample types and the range of measurements that can be accommodated. ROSI is primarily intended for reflectance measurements of spectrally neutral, non-fluorescent, highly reflective samples. The presence of the anodized aluminum sample holder behind the sample can affect reflectance measurement results if a sample is partially transmissive. However, it is also possible in some cases to mount the sample perpendicular to the sample holder for bidirectional transmittance distribution function (BTDF) measurements at limited geometries. Retroreflection measurements are not possible because the receiver blocks the incident

Table 2. System Capabilities

Goniometer Specifications		
Parameter	Specification	Notes
Robot type	Articulated arm	± 0.02 mm positioning repeatability
Number of axes	6	Enables full hemispherical scanning
Sample size	25 mm (min) to 300 mm (max)	Thickness 0 mm to 40 mm
Sample payload	3.5 kg nominal; 9 kg max	Including sample holder
Sample attachment	Mechanical or vacuum chuck	
Sample translation	± 75 mm from center	Nominal
Receiver arm rotation	360° about robot	
Receiver distance	658 mm	Nominal, see Section 4.2
Optical Specifications		
Parameter	Specification	Notes
Measurement types	Reflectance, BRDF, Reflectance Factor	Bidirectional transmittance distribution function (BTDF) at limited geometries
Measurement technique	Absolute	
Source type	Tunable SC or LDLS/monochromator	See Section 3.A
Wavelengths	250 nm–2400 nm	Quasi-monochromatic
Source bandwidth	14 nm	Full-width at half maximum (FWHM) bandwidth
Minimum wavelength step	10 nm	Recommended due to bandwidth
Incident beam diameter	10 mm	At normal incidence
Polarization	Linear incident	Rotatable
Detector types	Silicon, EIGA on integrating sphere	
Solid angle of collection	0.0026 sr	Nominal, subtends about 3.3°, see Section 4.2
Incident angle	$\theta_i = 0^\circ - 80^\circ$, $\phi_i = 0^\circ - 360^\circ$	Based on 10 mm incident beam
Viewing angle	$\theta_r = 0^\circ - 88^\circ$, $\phi_r = 0^\circ - 360^\circ$	Full hemispherical scanning, unobstructed view of sample, retroreflection excluded.

beam. For near retroreflection geometries, the minimum practical separation between incident and viewing angles is 4° . Additional sample and measurement parameters are listed in Table 2.

4. UNCERTAINTY CONSIDERATIONS

In this section we discuss the uncertainty components that determine the overall uncertainty in a measurement of specular reflectance, BRDF, or reflectance factor. The uncertainty has been broken into electrical, solid-angle, sample-dependent, and additional components. The electrical and solid-angle components follow directly from the uncertainty in input quantities that appear in the measurement equations, like signal or distance. Sample-dependent components arise from quantities that do not explicitly appear in the measurement equation, but upon which the measurand (BRDF or specular reflectance) is dependent. An example would be a wavelength-dependent BRDF, where a change in illumination wavelength changes the value of the measurand even though wavelength does not explicitly appear in Eq. (2). Following [14], additional components are components that do not change the magnitude of the measurand but do add uncertainty. Examples of this type of component are uniformity and stability. Referring to Eqs. (1)–(3), a specular reflectance measurement will be affected only by electrical, sample, and additional components, whereas measurements of BRDF or reflectance factor will also include uncertainty components related to solid angle.

A. Electrical

All measurements of reflectance, whether it be specular or diffuse, involve the ratio of the reflected radiant flux to the incident radiant flux, which we have represented as ρ in Eq. (1). Going into more detail, the incident and reflected flux at the goniometer receiver are measured using either the silicon or EIGA photodetector, a pre-amp, and a lock-in amplifier. In addition, a monitor channel, with its own detector, pre-amp, and lock-in amplifier, is used to compensate for any drift in the light source power. Therefore, in practice we measure ρ as

$$\rho = \frac{S_r}{S_i} = R_V \cdot R_G \cdot R_L, \quad (4)$$

where

$$R_V = \frac{V_{d,r}}{V_{m,r}} \cdot \frac{V_{m,i}}{V_{d,i}}. \quad (5)$$

The voltage ratio is R_V , where $V_{d,r}$ and $V_{m,r}$ are the voltages read by the receiver detector and monitor detector lock-ins during the reflected flux measurement, respectively, and $V_{d,i}$ and $V_{m,i}$ are the voltages read by the receiver detector and monitor detector lock-ins during the incident flux measurement, respectively. The additional terms in Eq. (4) are as follows. First, because we may change the gain of the receiver pre-amp between measurements of incident flux and reflected flux, especially for BRDF measurements where there are orders of magnitude difference in the reflected and incident signals, we must include R_G , the ratio of the receiver pre-amp gain during the incident

flux measurement to the receiver pre-amp gain during the reflected flux measurement. Similarly, R_L accounts for any difference in the voltage response of the receiver lock-in at the sensitivity settings used during the reflected and incident flux measurements. It is important to note that because reflectance is a ratio measurement, the absolute gains and sensitivities of the amplifiers and lock-ins need not be known, so long as the relative gains and sensitivities can be obtained. The values and uncertainties of R_G and R_L for all applicable gain and sensitivity settings were determined during the characterization of the instrument by comparing signal levels' output by adjacent gain or sensitivity settings for a range of input optical signals. The values of the uncertainty components $u(R_V)$, $u(R_G)$, and $u(R_L)$ depend upon the signal levels, pre-amp gain levels, and lock-in sensitivity levels used in a measurement. Typical values will be given in Section 5.

B. Solid Angle

Calculating BRDF or reflectance factor for a diffuse sample requires knowledge of the solid angle over which the diffuse scattering is collected. In the limit of uniform collection over an aperture of area A located a distance D away from an infinitesimally small illuminated spot of the sample surface, the geometric solid angle Ω is given by

$$\Omega = \frac{A}{D^2}. \quad (6)$$

In practice, the ideal geometric solid angle is modified by the surface projection angle and correction factors and is given by the effective projected solid angle Ω' introduced in Section 2.B,

$$\Omega' = \frac{A}{D^2} \cdot C_f \cdot C_e \cdot \cos \theta_r, \quad (7)$$

where θ_r is the viewing angle. The nominal values and standard uncertainties for A and D are $A = (1128.636 \pm 0.008) \text{ mm}^2$ and $D = (657.57 \pm 0.08) \text{ mm}$. The view angle θ_r depends on the measurement requirements but has a standard uncertainty of 0.05° . The uncertainties for D and θ_r are sometimes increased if the geometry of the sample adds additional uncertainty. C_f and C_e are near-unity correction factors that account for the effect of the finite size of the illuminated area and precision aperture on solid-angle projection, and for differences in collection efficiency for light filling the precision aperture when viewing reflected radiant flux compared to the collection efficiency for the near-collimated incident radiant flux, respectively.

The exact value of C_f depends on the geometry, including the incident and viewing angles [12], and is given by

$$C_f = 1 - \frac{R_a^2}{D^2} + \frac{R_i^2}{D^2} \frac{1}{\cos^2 \theta_i} \times \left[\cos(2\phi) \sin^2 \theta_i \sin^2 \theta_r - \cos(2\theta_r) \frac{3 + \cos(2\theta_i)}{4} \right], \quad (8)$$

where R_a is the radius of the receiver precision aperture; R_i is the radius of the incident illumination spot on the sample at normal incidence; A , D , θ_i , and θ_r are as previously defined;

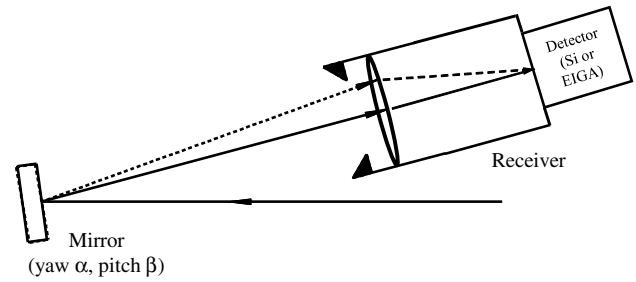


Fig. 5. Setup for scanning under-filling beam over receiver aperture to determine effective solid angle.

and $\phi = \phi_r - \phi_i$ is the difference between the azimuthal angles of incidence and viewing. For the 0/45 viewing geometry and an ideal uniform illumination spot, $C_f = 0.9992$. A standard relative uncertainty $u(C_f)/C_f$ of 0.05% is assigned to C_f , based upon numerical calculations of the variation of C_f given the nonuniformities in the actual illumination source.

The correction factor C_e is needed because the geometric solid angle assumes that the efficiency of light collection is the same regardless of whether light is collimated and goes through the center of the aperture or is diffuse and collected over the full aperture. If the optics behind the precision aperture, which include the lens and detector assemblies (for silicon and EIGA detectors) are not uniform in the way they transmit and collect the light, the need for a correction to the solid angle can result. We tested the uniformity of collection and determined C_e using a beam scanning technique. Briefly, a mirror was mounted on the ROSI sample holder, and the detector arm was positioned to collect the beam, which under-fills the detector aperture as shown in Fig. 5. Note that the distance from mirror to receiver has been greatly compressed in the figure to illustrate the measurement concept. The beam was scanned in pitch α and yaw β in a grid of uniform steps $\Delta\alpha$ and $\Delta\beta$ of 0.2° over the aperture. It can be shown that the effective solid angle Ω_{eff} measured by the scanning procedure is given by

$$\Omega_{\text{eff}} = \frac{4}{S_{00}} \sum_{\alpha, \beta} S_{\alpha\beta} \cos \alpha \cos^2 \beta \Delta\alpha \Delta\beta, \quad (9)$$

where S_{00} is the signal measured when the beam is passing through the center of the aperture (specular position), $S_{\alpha\beta}$ is the signal when the mirror is at angle pair (α, β) , and the angles are measured in radians. The beam scan was carried out at multiple wavelengths to get an average and standard deviation of Ω_{eff} for each detector: the directly illuminated silicon photodiode for the UV-NIR and the EIGA on a small integrating sphere for the SWIR. For each detector, we then calculated the correction factor C_e from

$$C_e = \frac{\Omega_{\text{eff}}}{\Omega}. \quad (10)$$

In the case of the integrating sphere-mounted EIGA detector, the collection efficiency for diffusely scattered light was about 0.6% higher than that for the collimated incident light that was centered on the precision aperture. In the case of the directly illuminated silicon detector, there was negligible difference

in the efficiency of diffusely scattered light compared to collimated incident light. Combining the standard deviation of the measurements of Ω_{eff} with the estimated accuracy of the model given the illumination beam size and step size of the scan, we conclude that $C_e = 1.0002$ and $u(C_e) = 0.0032$ for the silicon detector and $C_e = 1.0058$ with $u(C_e) = 0.0021$ for the EIGA detector on the sphere.

C. Sample-Dependent Components

While we have not explicitly shown it in Eqs. (1)–(3), the specular reflectance ρ , BRDF f_r , and reflectance factor R for practical samples are always dependent upon quantities that do not appear explicitly in the measurement equation, such as wavelength, polarization, and incident and viewing angles. For example, the BRDF for an in-plane measurement might depend upon incident angle, viewing angle, wavelength, and polarization: $f_r(\theta_i, \theta_r, \lambda, \sigma)$. If we label the quantities inside the parentheses as variables x_i , then following [1,10], the uncertainties $u(x_i)$ in these quantities lead to additional relative uncertainty components of the form

$$u_{\text{rel}}(x_i) = \frac{1}{f_r} \frac{\partial f_r}{\partial x_i} u(x_i), \quad (11)$$

which are added in quadrature to the other relative uncertainty components to calculate the relative standard uncertainty in f_r . Common x_i that give significant uncertainty components are wavelength, with $u(\lambda) = 0.7$ nm, and incident and viewing angles, with typical $u(\theta_i) = u(\theta_r) = 0.05^\circ$ (possibly larger if the sample mounting gives an increased angle uncertainty).

Another sample-dependent component is stray light, that is, light reaching the detector during incident or reflected light measurements that is not at the intended wavelength or that originates from any other unintended source. The relative uncertainty component due to stray light can be given generally as [1]

$$u_{\text{rel}}(q_i, q_r) = \frac{q_r - q_i}{1 + q_i}, \quad (12)$$

where q_i is the fraction of stray light $S_{i,\text{stray}}$ in the incident signal S_i , given by

$$q_i = \frac{S_{i,\text{stray}}}{S_i}, \quad (13)$$

and q_r is the fraction of stray light $S_{r,\text{stray}}$ in the reflected signal S_r , given by

$$q_r = \frac{S_{r,\text{stray}}}{S_r}. \quad (14)$$

For ROSI, the most significant stray light component is spectral stray light; that is, light in the incident beam that is not at the signal wavelength. A full accounting for the stray light effects must take into consideration the spectrum of the stray light, the wavelength-dependent responsivity of the detector, and the dependence of the sample reflectance on wavelength. For spectrally neutral samples, $q_i = q_r$, and the stray light uncertainty is negligible. This is generally the case for measurements

performed as calibrations. However, for research applications where the signal may be in a region of relatively low sample reflectance and detector responsivity, stray light effects can be significant.

Finally, the value of BRDF, reflectance, or reflectance factor may be dependent upon position on the sample. This is expressed as a sample uniformity uncertainty $u(U_s)$, which is evaluated from the standard deviation of the measurand at multiple points on the sample and leads to a relative uncertainty component

$$u_{\text{rel}}(U_s) = \frac{1}{f_r} u(U_s). \quad (15)$$

D. Additional Uncertainty Components

Additional uncertainty components are components that do not affect the value of the measurand, do not appear explicitly in the measurement equation, but nonetheless add uncertainty [14]. These components are modeled as multiplicative factors to the measurement equation with a value of unity, so the standard uncertainty and the relative standard uncertainty are the same. The first such component is receiver/monitor gain ratio stability $u(R_S)$, which accounts for any drift of the relative responsivity and pick-off efficiency between the receiver and monitor detectors between incident and reflected flux measurements. The value of $u(R_S)$ was determined to be 0.04% for the silicon detector and 0.08% for the EIGA detector from stability measurements made over multiple hours representative of the typical measurement times. Next, detector uniformity contributes to reflectance/scatter uncertainty because different parts of the silicon detector, or different areas of the sphere wall for the EIGA detector, are illuminated during the total flux and scatter/reflected signal measurements. For specular measurements, the detector uniformity uncertainty $u(U_D)$ was found to be 0.04% for the silicon detector and 0.01% for the EIGA detector on the sphere. In the case of diffuse measurements (BRDF or reflectance factor) the detector uniformity uncertainty is included as part of the receiver collection efficiency uncertainty $u(C_e)$ discussed in Section 4.B. Finally, an additional component for diffuse measurements, $u(C_I)$ (illumination centering), arises from our imperfect ability to center the illumination beam in the goniometer. This component is calculated from the uncertainty in illumination position and is incident and viewing-angle dependent. The calculation is shown in Appendix A.

E. Combined Relative Uncertainty

The calculation of combined relative uncertainty for a measurement of reflectance, BRDF, or reflectance factor follows the rules for propagation of uncertainty [15]. We demonstrate the calculation for BRDF because it includes all categories of uncertainty components including the solid-angle components. Following the discussion in Sections 4.A through 4.D, we have

$$\begin{aligned} \frac{u^2(f_r)}{f_r^2} &= \frac{u^2(R_V)}{R_V^2} + \frac{u^2(R_G)}{R_G^2} + \frac{u^2(R_L)}{R_L^2} + \frac{u^2(A)}{A^2} \\ &+ \frac{4u^2(D)}{D^2} + \frac{u^2(C_i)}{C_i^2} + \frac{u^2(C_e)}{C_e^2} \\ &+ \left(\frac{1}{f_r} \frac{\partial f_r}{\partial \theta_r} - \tan \theta_r \right)^2 u^2(\theta_r) + \sum_i \left[\frac{1}{f_r} \frac{\partial f_r}{\partial x_i} u(x_i) \right]^2 \\ &+ u_{rel}^2(q_i, q_r) + u_{rel}^2(U_s) + u^2(R_s) + u^2(C_1). \end{aligned} \tag{16}$$

An example uncertainty budget for reflectance factor, which has the same uncertainty components as BRDF, is shown in Section 5.B. Each relative uncertainty contribution is the square root of one of the components in Eq. (16); however, some components, like the stray light component $u_{rel}(q_i, q_r)$, were negligible for the example measurement and are not represented.

Two clarifications to Eq. (16) are in order. First, as discussed in Ref. [10], including a $\partial f_r / \partial \theta_r$ term along with the $\tan \theta_r$ preceding the uncertainty component $u^2(\theta_r)$ avoids double counting the effect of $u(\theta_r)$ for samples where the BRDF has a strong dependence upon viewing angle. For reasonably Lambertian samples, the viewing angle dependence of f_r is negligible and the $\tan \theta_r$ dominates.

Second, in Section 3.A we noted that the incident beam in ROSI is linearly polarized. In many cases, we are ultimately interested in the unpolarized reflectance. If we denote the BRDF for p -polarized light as $f_{r,p}$ and that for s -polarized light as $f_{r,s}$, then the unpolarized BRDF is

$$f_{r,unpol} = \frac{1}{2} (f_{r,p} + f_{r,s}). \tag{17}$$

When we calculate the uncertainty for $f_{r,unpol}$, we must consider that most of the uncertainty components for the individual s - and p -polarized measurements that are shown in Eq. (16), except the voltage noise component $u(R_V)$, are highly correlated between the two measurements. Since BRDF measurement accuracy is generally not noise limited, we make the approximation that $u(f_{r,p})$ and $u(f_{r,s})$ are correlated, so the resulting uncertainty $u(f_{r,unpol})$ is [15]

$$u(f_{r,unpol}) = \frac{1}{2} (u(f_{r,p}) + u(f_{r,s})). \tag{18}$$

In the case of most white, Lambertian samples, $u(f_{r,p})$ is approximately equal to $u(f_{r,s})$, so using Eq. (18), the uncertainty for the unpolarized measurement $u(f_{r,unpol})$ is also approximately equal to $u(f_{r,p})$ or $u(f_{r,s})$.

5. REFERENCE REFLECTOR MEASUREMENTS

ROSI serves as the national reference instrument for specular and bidirectional diffuse reflectance measurements. In this section, we present two common types of reference standard measurements and their typical uncertainties. We also show the residuals between ROSI and STARR, the previous reference instrument, for measurements of typical sample types.

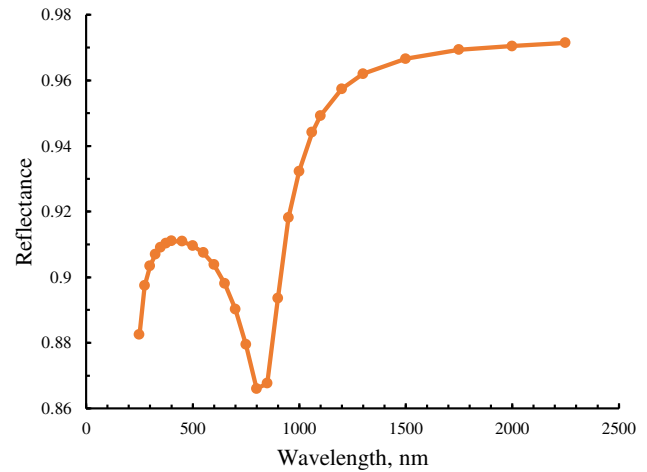


Fig. 6. Unpolarized reflectance of the protected aluminum mirror described in the text. The $k = 2$ uncertainty in the points is typically 0.0013 for wavelengths below 1000 nm and 0.0016 for wavelengths 1000 nm and above. Error bars (not shown) would be similar in size to the symbols on the plot. Uncertainty budget components are given in Table 3.

A. Specular Reflectance Measurement and Uncertainty

Figure 6 shows the results for unpolarized reflectance versus wavelength for a protected aluminum mirror in the $6/ - 6$ geometry. This is a common type of commercial mirror that is also used as a reference standard mirror. Reflectance is calculated using Eq. (1). The dip in reflectance around 800 nm is typical of protected aluminum [16].

Table 3 shows typical relative uncertainty contributions ($k = 1$) for reflectance measurement of a protected aluminum mirror. The expanded uncertainty ($k = 2$), following Eq. (16) and replacing f_r with ρ , is the combined (root-sum-square) uncertainty of the relative uncertainty contributions due to systematic and random effects, multiplied by the reflectance factor to obtain absolute uncertainty, and then multiplied by a coverage factor of 2. As seen in the table, the uncertainty budget for specular measurements has fewer components than that for BRDF, since many components seen in Eq. (16) are not represented.

B. Comparison with STARR

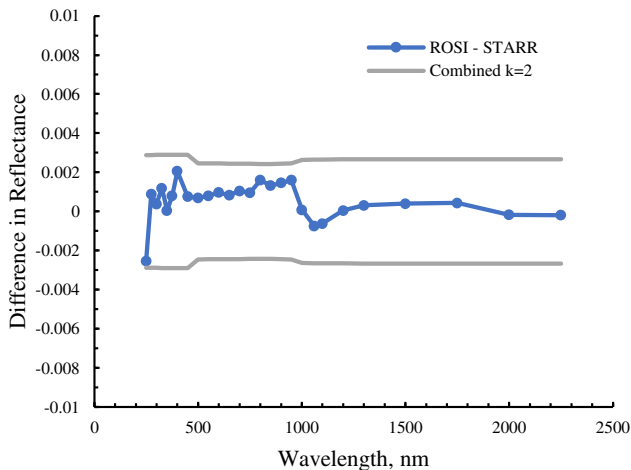
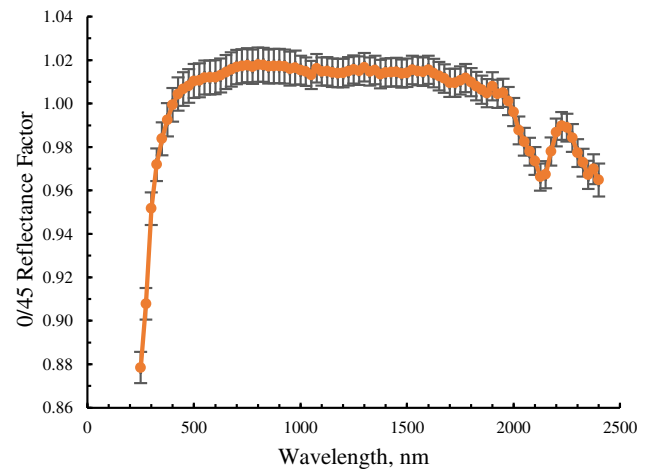
As part of the validation for ROSI, the reflectance of the aluminum mirror from Fig. 6 was measured on both ROSI and STARR. The results for the residual difference between the ROSI and STARR measurements, along with the combined $k = 2$ uncertainty for the two instruments, are shown in Fig. 7. Residuals are within the combined $k = 2$, indicating good agreement between the two facilities.

C. 0/45 Reflectance Factor Measurement and Uncertainty

Reflectance factor in the 0/45 geometry is the most common measurement made for diffuse reference reflectors. Referring to Fig. 1, the measurement is made at 0° incidence, 45° view

Table 3. Nominal Relative Uncertainty Contributions ($k = 1$) as a Function of Wavelength λ for the Reflectance ρ of a Protected Aluminum Mirror

Source of Uncertainty	Standard Uncertainty	Relative Uncertainty Expression	Relative Uncertainty Contribution
Receiver/Monitor Gain Ratio Stability		$u(R_S)$	
250 nm $\leq \lambda \leq$ 990 nm	0.04%		0.0004
1000 nm $\leq \lambda \leq$ 2400 nm	0.08%		0.0008
Detector Uniformity		$u(U_D)$	
250 nm $\leq \lambda \leq$ 990 nm	0.04%		0.0004
1000 nm $\leq \lambda \leq$ 2400 nm	0.01%		0.0001
Detector Noise		$u(R_V)/R_V$	
250 nm $\leq \lambda \leq$ 990 nm	<0.01%		<0.0001
1000 nm $\leq \lambda \leq$ 2400 nm	<0.01%		<0.0001
Wavelength		$\frac{1}{\rho} \frac{\partial \rho}{\partial \lambda} u(\lambda)$	
250 nm	0.7 nm		0.0004
260 nm $\leq \lambda \leq$ 840 nm	0.7 nm		0.0001
850 nm $\leq \lambda \leq$ 1050 nm	0.7 nm		0.0003
1060 nm $\leq \lambda \leq$ 2400 nm	0.7 nm		<0.0001
Sample Uniformity		$u_{rel}(U_s)$	0.0002
Sample Alignment	0.05°	$\frac{1}{\rho} \frac{\partial \rho}{\partial \theta_i} u(\theta_i)$	<0.0001

**Fig. 7.** Residual between unpolarized reflectance measured by ROSI and STARR for a first surface protected aluminum mirror.**Fig. 8.** 0/45 reflectance factor measured by ROSI for the diffuse sample described in the text. Error bars are $k = 2$.

geometry (0/45) as a function of wavelength, and the reflectance factor is calculated from scattered flux measurements using Eq. (3).

Figure 8 shows the 0/45 reflectance factor for a sintered polytetrafluoroethylene (PTFE) sample, measured at wavelengths from 250 to 2400 nm, along with the expanded uncertainty ($k = 2$) at each point. The expanded uncertainty is the combined (root-sum-square) uncertainty of the relative uncertainty contributions due to systematic and random effects, multiplied by the reflectance factor to obtain absolute uncertainty, and then multiplied by a coverage factor $k = 2$. The typical uncertainty components for 0/45 reflectance factor are shown in Table 4.

D. Comparison with STARR

The sample whose data is shown in Fig. 8 was also measured using the STARR instrument. Figure 9 shows the residual

difference between reflectance factor values measured by ROSI and STARR from 300 to 2400 nm, along with the combined $k = 2$ uncertainty of the measurements. The agreement is within the combined uncertainty for most of the wavelength range. For wavelengths below 300 nm, agreement between STARR and ROSI was less consistent. At these wavelengths, the reproducibility of STARR measurements for diffuse samples was known to be limited by low source flux, and the uncertainty of the STARR measurements was several percent. The higher source flux in ROSI has greatly improved the uncertainty of reflectance factor results in the UV.

6. INSTRUMENT SIGNATURE AND OUT-OF-PLANE MEASUREMENTS

In this section, we first consider the reflectance measurement limits of ROSI, expressed as the instrument signature.

Table 4. Nominal Relative Uncertainty Contributions ($k = 1$) as a Function of Wavelength λ of the Reflectance Factor R of a Sintered PTFE Sample

Source of Uncertainty	Standard Uncertainty	Relative Uncertainty Expression	Relative Uncertainty Contribution
Aperture Distance	0.09 mm	$2u(D)/D$	0.0003
Aperture Area	0.77 mm ²	$u(A)/A$	<0.0001
Finite Solid Angle Calculation	0.05%	$u(C_f)/C_f$	0.0005
Viewing Angle	0.05°	$\frac{1}{f_r} \frac{\partial f_r}{\partial \theta_r} - \tan \theta_r$	0.0009
Illumination Centering	0.5 mm	$u(C_I)$	0.0016
Detector Gain Ratio		$u(R_G)/R_G$	
$\lambda < 1050$ nm	0.06%		0.0006
$\lambda \geq 1050$ nm	0.03%		0.0003
Lock-in Amplifier Sensitivity Ratio		$u(R_L)/R_L$	
$\lambda < 1050$ nm	0.02%		0.0002
$\lambda \geq 1050$ nm	0.15%		0.0015
Receiver/Monitor Gain Ratio		$u(R_S)$	
Stability			
$\lambda < 1050$ nm	0.04%		0.0004
$\lambda \geq 1050$ nm	0.08%		0.0008
Receiver Efficiency Uniformity		$u(C_e)/C_e$	
$\lambda < 1050$ nm	0.32%		0.0032
$\lambda \geq 1050$ nm	0.21%		0.0021
Detector Noise		$u(R_V)/R_V$	
$\lambda < 1050$ nm	0.01%		0.0001
1050 nm $\leq \lambda < 2300$ nm	0.05%		0.0005
2300 nm $\leq \lambda < 2400$ nm	0.3%		0.003
$\lambda = 2400$ nm	0.9%		0.009
Wavelength	0.7 nm	$\frac{1}{f_r} \frac{\partial f_r}{\partial \lambda} u(\lambda)$	
$\lambda < 325$ nm			0.0013
325 nm $\leq \lambda < 425$ nm			0.0004
425 nm $\leq \lambda < 1900$ nm			<0.0001
$\lambda \geq 1900$ nm			0.0002
Sample Uniformity	0.07%	$u_{rel}(U_s)$	0.0007
Incident Angle	0.05°	$\frac{1}{f_r} \frac{\partial f_r}{\partial \theta_i} u(\theta_i)$	<0.0001

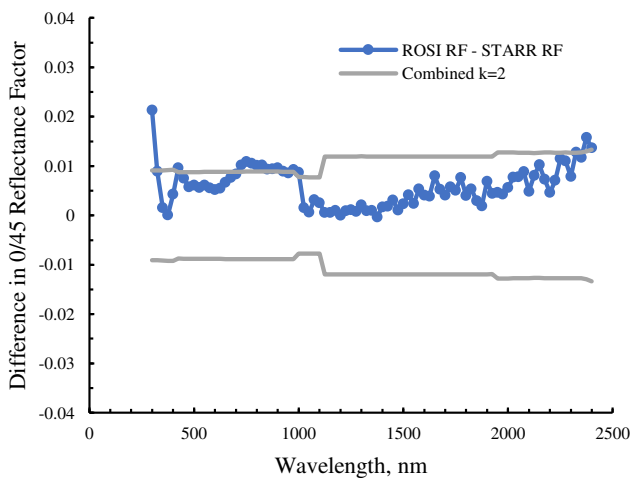


Fig. 9. Residual between 0/45 reflectance factor measured by ROSI and STARR for the diffuse sample described in the text, along with the combined $k = 2$, 300 nm to 2400 nm.

The instrument signature determines the lowest specular and bidirectional measurements that can be practically made on ROSI. We then consider a research application for the

out-of-plane measurement capability of the instrument, using as an example the needs of the remote sensing community for out-of-plane reflectance factor measurements of diffuse reference targets.

A. Instrument Signature

The instrument signature is the minimum measurable reflectance and varies with the detector and light source combination (see Table 1). We evaluated the instrument signature with the detector in the 0/45 position with no sample in the beam, the sample holder dropped well below the beam position, and a light trap positioned beyond the goniometer to capture the incident beam. Figure 10 shows the instrument signature for measurements made using the silicon detector. The instrument signature for specular reflectance ρ is obtained directly from the ratio of signal with no sample present to incident signal using Eq. (1), and the instrument signature for 0/45 reflectance factor is calculated from that ratio using Eq. (3). The relative magnitude of the uncertainty in the instrument signature varies with the light source and detector; the lowest uncertainty is seen for points in the range where the supercontinuum source and silicon detector are used, with larger uncertainties due to higher

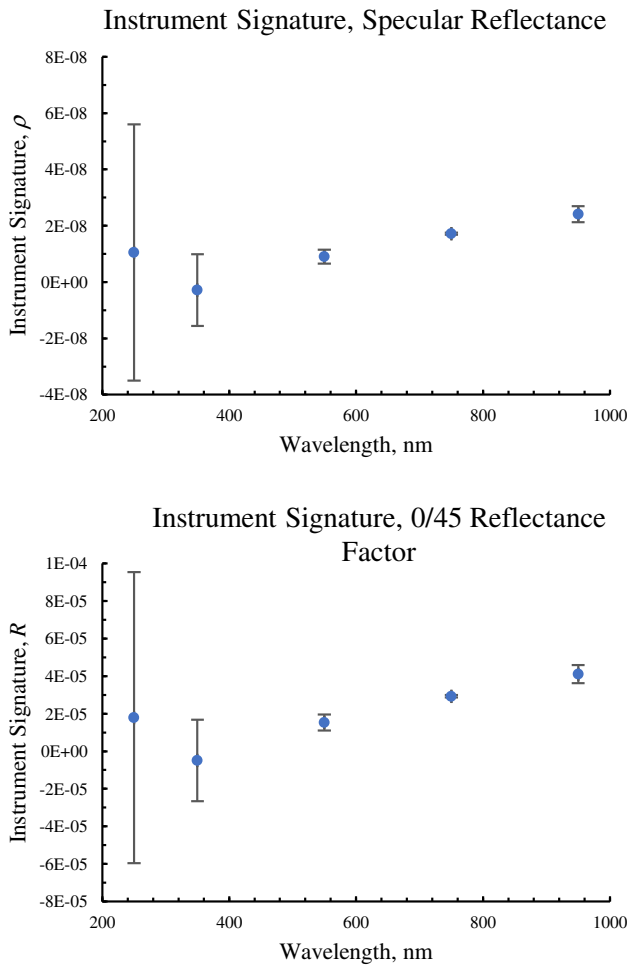


Fig. 10. Instrument signature for specular reflectance (top) and 0/45 reflectance factor (bottom) measured as described in the text. Error bars are $k = 1$.

noise levels for the LDLS and silicon detector (below 500 nm). Nonetheless, the measurements indicate the ability to measure specular reflectance down to the level of 5×10^{-8} and 0/45 reflectance factor down to 0.0001 using the silicon detector. For measurements made using the supercontinuum and EIGA detector on a sphere (not shown in Fig. 10), the instrument signature is higher due to the attenuation from the detector sphere. We estimate that at 2200 nm, where we use the supercontinuum source and the EIGA detector, the instrument signature for a reflectance factor measurement in the 0/45 geometry is less than or equal to 0.0005.

B. Out-of-Plane Reflectance Factor for Remote Sensing

A major enhancement of the ROSI instrument over the previous STARR facility is the ability of ROSI to measure bidirectional diffuse reflectance for out-of-plane geometries. One application of this feature is in the characterization of white or gray sintered PTFE targets as reference reflectors for remote sensing studies of water color. A typical protocol is to measure the reference target with the sun at an angle between 0° to 70° from zenith in polar angle, and the sensor with a polar angle around 40° and

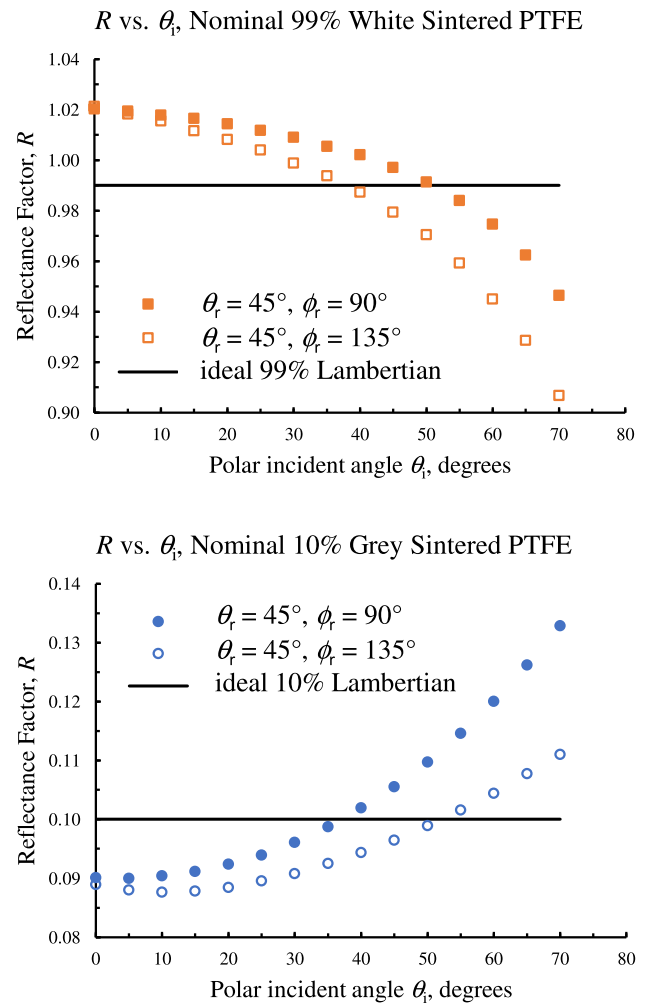


Fig. 11. Reflectance factor versus polar incident angle for a nominal 99% reflectance white sintered PTFE target (top) and a nominal 10% reflectance gray sintered PTFE target (bottom) as described in the text.

at a large azimuthal angle—for example, 90° or 135° —from the incident plane formed by the solar incident direction and the target normal [9,17]. Referring to Fig. 2, this corresponds to the sun with incident polar angles $0^\circ \leq \theta_i \leq 70^\circ$ and incident azimuthal angle $\phi_i = 180^\circ$, and the viewing sensor at polar angle $\theta_r = 40^\circ$ and azimuthal angle $\phi_r = 90^\circ$ or $\phi_r = 135^\circ$. It is often assumed that the reference target is Lambertian—perfectly diffuse—so the bidirectional reflectance factor R [see Eq. (3)] at any combination of incident and viewing angles is a constant and equivalent to the directional/hemispherical reflectance supplied by the vendor [18]. The directional/hemispherical reflectance is a unitless reflectance that is measured for a specific incident angle, integrated over all viewing angles in a hemisphere above the sample, and it is equal to 1 for a PRD. In the following discussion we refer to the manufacturer's specified directional/hemispherical reflectance as the nominal reflectance of the sample.

To test the potential uncertainty introduced by this assumption, we measured the bidirectional reflectance factor for two types of sintered PTFE reference targets: a 99% nominal reflectance white, and a 10% nominal reflectance gray, at varying polar incident angle and two fixed out-of-plane viewing

configurations. The results are shown in Fig. 11. For this data, the polar incident angle θ_i was varied from 70° to 0° to simulate illumination of the target by the sun as it tracks from low in the sky to zenith, with the azimuthal incidence angle fixed at $\phi_i = 180^\circ$. Two viewing configurations were investigated: $\theta_r = 45^\circ$ with azimuthal angle $\phi_r = 90^\circ$ and $\theta_r = 45^\circ$ with $\phi_r = 135^\circ$. All measurements were made using an illumination wavelength of $\lambda = 550$ nm. Also shown on the graphs are the reflectance factor that would be assumed were the targets perfectly Lambertian; that is, constant reflectance factor of 0.99 for the white target and 0.10 for the gray target. For both viewing azimuths, both the white and gray targets deviate from Lambertian, particularly at large incident angles. The precise mechanism for the deviation is not well understood. For the white sample, similar variations with viewing geometry have been seen in white pressed PTFE, a very similar material [19]. The BRDF/reflectance factor of gray sintered PTFE has not been as widely studied, but it is generally known to show different variation from Lambertian compared to white sintered PTFE [20]. We roughly estimate the relative expanded uncertainty $k = 2$ for the data shown in Fig. 11 to be 0.01 of the reflectance factor value for measurements on the white target and 0.02 of the reflectance factor value of the gray target, with out-of-plane measurements expected to include larger uncertainty components for angle accuracy and solid angle than that shown for in-plane calibrations. The results show that errors of greater than 30% for the reference reflector value would be generated if the Lambertian assumption was used on a gray target with 90° viewing azimuth, while use of a white reference or different viewing geometry reduces the error incurred by assuming Lambertian behavior, reducing the uncertainty of the reference measurement to desired levels of a few percent requires knowledge of the bidirectional reflectance and careful choice of viewing geometry [17]. Measurements like these, along with thorough theoretical investigation of the influence of the BRDF of the targets on remote sensing measurements, will enable improvements in the quality of measurements and the knowledge of the true remote sensing uncertainty.

7. SUMMARY AND OUTLOOK

In this paper we have reported on ROSI, the national reference instrument for specular and bidirectional spectral reflectance measurements. The development of ROSI enables NIST to maintain reflectance scales and calibration capabilities important to industrial, government, and academic stakeholders that were previously carried out in the STARR facility, such as specular spectral reflectance and 0/45 reflectance factor, in the UV-SWIR wavelength range. Additionally, the increased light source flux and the ability of the robotic arm goniometer to reach nearly any combination of incident and viewing angles enables ROSI to access new applications, such as low-reflectance diffuse materials [21], and to make measurements at out-of-plane geometries, for example, replicating geometries used in the field by the remote sensing community [17]. Going forward, we anticipate increased use and characterization of the instrument for out-of-plane BRDF measurements over the full hemisphere, such as those needed for modeling reflectance and appearance of materials with both diffuse and

specular components. We are also in the process of validating an 8/di (8° incidence, diffuse reflectance with specular included) integrating sphere for directional/hemispherical reflectance measurements that employs the same tunable light source as the robot goniometer. Currently, directional/hemispherical calibrations are made in the STARR facility. The addition of the 8/di integrating sphere will allow all calibrations historically performed in STARR to be transitioned to ROSI. The development of ROSI has been vital for the ongoing validation of customer reflectance scales and represents a significant expansion of NIST’s capabilities for research in spectral bidirectional reflectance.

APPENDIX A: EXPRESSION FOR ILLUMINATION CENTERING UNCERTAINTY

As shown in Eq. (7), calculating the effective solid angle for measuring BRDF or reflectance factor requires knowing the distance and viewing angle of the receiver from the goniometer center. The uncertainty components $u(D)$ and $u(\theta)$ represent the standard uncertainties in these quantities. However, there is an additional uncertainty component $u(C_I)$ arising from the fact that while the goniometer may be very well aligned, with small $u(D)$ and $u(\theta)$, our ability to direct the illumination exactly to the goniometer center is imperfect. Referring to Fig. 12, if the incident beam is shifted from the center of the sample by a distance a , it can be shown that rather than measuring at distance D and viewing angle θ_r , the receiver in fact measures at distance D_a and angle θ_a , where

$$\theta_a = \tan^{-1} \left[\frac{D \sin \theta_r - a}{D \cos \theta_r} \right] \tag{A1}$$

and

$$D_a = \sqrt{D^2 \cos^2 \theta_r + (D \sin \theta_r - a)^2}. \tag{A2}$$

Note that Fig. 12 shows the condition for normal incidence illumination. For non-normal incident angle, we must replace a with $a / \cos \theta_i$ in Eqs. (A1) and (A2).

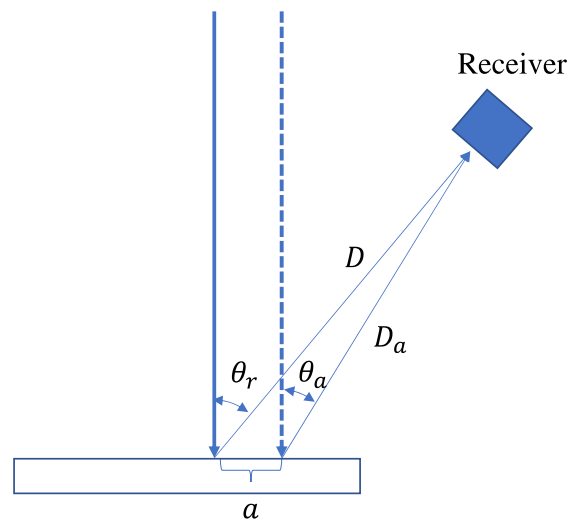


Fig. 12. Geometry for calculating illumination centering uncertainty.

If a is taken to be the standard uncertainty in the illumination center position, then the standard uncertainty from illumination centering $u(C_I)$ is

$$u(C_I) = \left| 1 - \frac{\cos \theta_a}{\cos \theta_r} \cdot \frac{D^2}{D_a^2} \right|. \quad (\text{A3})$$

The illumination centering uncertainty is incident and viewing-angle dependent; as an example, for $a = 0.5$ mm and a 0/45 geometry, $u(C_I) = 0.0016$.

Acknowledgment. We thank Aaron Goldfain and Ronald Dixson of NIST for helpful discussions and comments on the paper. We also appreciate the contributions of the anonymous reviewers for improving our paper. We thank the National Institute of Standards and Technology for funding this research.

Disclosures. The authors declare no conflicts of interest.

Data Availability. Data underlying the results presented in this paper are not publicly available at this time but may be obtained from the authors upon reasonable request.

REFERENCES

1. P. Y. Barnes, E. A. Early, and A. C. Parr, "Spectral reflectance," NIST Special Publication 250-48 (NIST, 1998).
2. F. E. Nicodemus, J. C. Richmond, J. J. Hsia, I. W. Ginsberg, and T. Limberis, "Geometrical considerations and nomenclature for reflectance," NBS Monograph 160 (1977).
3. C. C. Cooksey, D. W. Allen, B. K. Tsai, and H. W. Yoon, "Establishment and application of the 0/45 reflectance factor scale over the shortwave infrared," *Appl. Opt.* **54**, 3064–3071 (2015).
4. C. C. Cooksey, M. E. Nadal, D. W. Allen, K.-O. Hauer, and A. Höpe, "Bidirectional reflectance scale comparison between NIST and PTB," *Appl. Opt.* **54**, 4006–4015 (2015).
5. G. Obein, R. Bousquet, and M. E. Nadal, "New NIST reference goniospectrometer," *Proc. SPIE* **5880**, 58800T (2005).
6. D. Huenerhoff, U. Grusemann, and A. Hoepfe, "New robot-based gonireflectometer for measuring spectral diffuse reflection," *Metrologia* **43**, S11–S16 (2006).
7. R. Baribeau, W. S. Neil, and E. Côté, "Development of a robot-based gonireflectometer for spectral BRDF measurement," *J. Mod. Opt.* **56**, 1497–1503 (2009).
8. H. J. Patrick, C. J. Zarobila, and T. A. Germer, "The NIST Robotic Optical Scatter Instrument (ROSI) and its application to BRDF measurements of diffuse reflectance standards for remote sensing," *Proc. SPIE* **8866**, 886615 (2013).
9. C. D. Mobley, "Estimation of the remote-sensing reflectance from above-surface measurements," *Appl. Opt.* **38**, 7442–7455 (1999).
10. T. A. Germer, J. C. Stover, and S. Schröder, "Angle-resolved diffuse reflectance and transmittance," in *Spectrophotometry: Accurate Measurement of Optical Properties of Materials*, T. A. Germer, J. C. Zwinkels, and B. K. Tsai, eds. (Academic, 2014), Chap. 8, pp. 291–331.
11. T. A. Germer, J. C. Zwinkels, and B. K. Tsai, "Theoretical concepts in spectrophotometric measurements," in *Spectrophotometry: Accurate Measurement of Optical Properties of Materials*, T. A. Germer, J. C. Zwinkels, and B. K. Tsai, eds. (Academic, 2014), Chap. 2, pp. 11–66.
12. H. J. Patrick, C. J. Zarobila, T. A. Germer, V. A. Ying, C. A. Cooksey, and B. K. Tsai, "Tunable supercontinuum fiber laser source for BRDF measurements in the STARR II gonireflectometer," *Proc. SPIE* **8495**, 84950K (2012).
13. "About lock-in amplifiers," 2020, <https://www.thinksrs.com/downloads/pdfs/applicationnotes/AboutLIAs.pdf>.
14. "IES technical memorandum on measurement uncertainty for lighting equipment calibration using integrating spheres (TM-31-17)," IES TM-31-17 (Illumination Engineering Society, 2018).
15. B. N. Taylor and C. E. Kuyatt, "Guidelines for evaluating and expressing the uncertainty of NIST measurement results," NIST Technical Note 1297 (1994).
16. V. R. Weidner and J. J. Hsia, "National Bureau of Standards Certificate, standard reference material 2003c, first surface aluminum mirror for specular reflectance from 250 nm to 2500 nm," 2021, <https://www-s.nist.gov/srmors/certificates/archives/2003c.pdf>.
17. A. Castagna, B. C. Johnson, K. Voss, H. M. Dierssen, H. Patrick, T. A. Germer, K. Sabbe, and W. Vyverman, "Uncertainty in global downwelling plane irradiance estimates from sintered polytetrafluoroethylene plaque radiance measurements," *Appl. Opt.* **58**, 4497–4511 (2019).
18. D. Doxoran, N. C. Cherukuru, S. J. Lavender, and G. F. Moore, "Use of a Spectralon panel to measure the downwelling irradiance signal: case studies and recommendations," *Appl. Opt.* **43**, 5981–5986 (2004).
19. T. A. Germer, "Full four-dimensional and reciprocal Mueller matrix bidirectional reflectance distribution function of sintered polytetrafluoroethylene," *Appl. Opt.* **56**, 9333–9340 (2017).
20. G. T. Georgiev and J. J. Butler, "BRDF study of gray-scale spectralon," *Proc. SPIE* **7081**, 708107 (2008).
21. J. Lehman, E. Theocharous, G. Eppeldauer, and C. Pannell, "Gold-black coatings for freestanding pyroelectric detectors*," *Meas. Sci. Technol.* **14**, 916–922 (2003).